

Cite this: *Phys. Chem. Chem. Phys.*, 2012, **14**, 14207–14216

www.rsc.org/pccp

PAPER

# Theoretical insight into the aggregation induced emission phenomena of diphenyldibenzofulvene: a nonadiabatic molecular dynamics study

Xing Gao,<sup>a</sup> Qian Peng,<sup>b</sup> Yingli Niu,<sup>b</sup> Dong Wang<sup>\*a</sup> and Zhigang Shuai<sup>\*ab</sup>

Received 4th February 2012, Accepted 20th March 2012

DOI: 10.1039/c2cp40347a

The diphenyldibenzofulvene (DPDBF) molecule appears in two forms: ring open and ring closed. The former fluoresces weakly in solution, but it becomes strongly emissive in the solid phase, exhibiting an exotic aggregation-induced emission phenomenon. The latter presents a normal aggregation quenching phenomenon, as is expected. We implement nonadiabatic molecular dynamics based on the combination of time-dependent Kohn–Sham (TDKS) and density functional tight binding (DFTB) methods with Tully's fewest switches surface hopping algorithm to investigate the excited state nonradiative decay processes. From the analysis of the nonadiabatic coupling vectors, it is found that the low frequency twisting motion in the ring open DPDBF couples strongly with the electronic excitation and dissipates the energy efficiently. While in the closed form, such motion is blocked by a chemical bond. This leads to the nonradiative decay rate for the open form (1.4 ps) becoming much faster than the closed form (24.5 ps). It is expected that, in the solid state, the low frequency motion of the open form will be hindered and the energy dissipation pathway by nonradiative decay will be slowed, presenting a remarkable aggregation enhanced emission phenomenon.

## I. Introduction

The aggregation-induced emission (AIE) phenomenon<sup>1,2</sup> presents a novel possibility to improve the performance of organic electronic devices, such as highly efficient organic light emitting materials,<sup>3–5</sup> fluorescence sensors<sup>6–11</sup> and bio-imaging agents.<sup>12–14</sup> Several kinds of organic molecules have been found to exhibit AIE properties, such as siloles,<sup>15</sup> tetraphenyl-ethene derivatives<sup>16</sup> and dibenzofulvene derivatives<sup>17,18</sup> *etc.* In general, molecular aggregation tends to quench luminescence due to intermolecular charge or energy transfer or Davydov splitting, which often stabilizes the dark component. It is intriguing to understand, and eventually predict, such exotic light-emitting behavior *via* computational chemistry.

Previously, based on the vibration correlation function formalism coupled with first-principles calculations under the displaced/distorted harmonic oscillator approximation, the radiative and nonradiative decay rates for molecules with AIE properties have been investigated. The important role of mode mixing caused by the Duschinsky rotation in nonradiative decay processes has been highlighted.<sup>19–25</sup> The solid state

packing effects on both radiative and non-radiative decay have been revealed by a combined quantum mechanics and classical mechanics (QM/MM) study, where the active light-emitting molecule was treated quantum mechanically and the surroundings were treated *via* classical mechanics with the two interacting through electrostatic potentials.<sup>26</sup> All of these studies pointed out the role of low frequency motion in the nonradiative decay process, namely, that the aggregation tends to vastly slow down the nonradiative decay process, giving way to the less affected radiative decay process. In fact, for low frequency vibrations, not only Duschinsky rotation and the mode distortion effect come in to play. Anharmonicity must also be considered. In addition, microscopic access to understand the detailed motion of electrons and nuclei, as well as electron–phonon interactions during the nonradiative decay process, from a dynamical point of view is highly desired for AIE molecules, which is beyond the reach of the conventional rate formalism. In this work, we employ a nonadiabatic dynamic approach to investigate the nonradiative decay processes for AIE molecules. Recent advances in semi-classical nonadiabatic dynamics, such as Ehrenfest and trajectory surface hopping (TSH) dynamics<sup>27–32</sup> have been remarkable, which treat the fast and slow degrees of freedom by quantum and classical mechanics, respectively, providing a computationally tractable route to investigate the AIE phenomena. The TSH dynamics combined with on-the-fly quantum chemistry calculations, like multi-reference methods, have been used to study photophysical and photochemical processes with

<sup>a</sup> MOE Key Laboratory of Organic OptoElectronics and Molecular Engineering, Department of Chemistry, Tsinghua University, Beijing, 100084, P. R. China. E-mail: dong913@tsinghua.edu.cn, zgshuai@tsinghua.edu.cn

<sup>b</sup> Key Laboratory of Organic Solids, Beijing National Laboratory for Molecular Science (BNLMS), Institute of Chemistry, Chinese Academy of Sciences, Beijing, 100190, P. R. China

conical intersections.<sup>33–42</sup> To enhance the computational efficiencies, wave function-based semi-empirical multi-reference methods, such as OM2/MRCI,<sup>43–45</sup> as well as single reference methods like AM1/CIS<sup>46,47</sup> and AM1/SCF-CI<sup>48,49</sup> have been incorporated into TSH dynamics. The combination of TSH with TDDFT, which performs well in some model systems, such as protonated formaldehyde,<sup>50</sup> oxirane,<sup>51</sup> pyrazine<sup>52</sup> and indole in water<sup>53</sup> provides a very promising route in the treatment of relatively large systems. More approximate but computationally cost efficient methods, such as TDKS<sup>54–58</sup> and restricted open-shell Kohn–Sham (ROKS)<sup>59–61</sup> methods, have been reported. In particular, many interesting systems, like semiconductor quantum dots<sup>54</sup> and chromophore–TiO<sub>2</sub>,<sup>56</sup> have been tested based on TDKS. The recent advances in density functional with tight binding approximation (DFTB) methods have been successful in the calculation of large systems.<sup>62–64</sup> It has been extended to time-dependent (TD-DFTB) schemes<sup>65</sup> and used to simulate a system composed of adenine solvated by 26 water molecules in the framework of TSH.<sup>66</sup> In addition, DFTB-based Ehrenfest dynamics have also been reported.<sup>67–71</sup> The advantage of TSH lies in the satisfaction of the detailed balance requirement,<sup>72,73</sup> as well as the capacity to trace the interested trajectories and recover the pure adiabatic states.<sup>30</sup>

In this study, to further accelerate the computational speed in relatively large molecular systems to a time scale of  $\sim 100$  ps, we incorporate TDKS and DFTB with Tully's fewest switches surface hopping (FSSH) algorithm<sup>74,75</sup> in nonadiabatic dynamics. Under this framework, we investigate the detailed nonradiative decay processes for open- and closed-DPDBF. From the ensembles of the trajectories in the nonadiabatic and Born–Oppenheimer dynamics, the results, such as the evolution of electrons and nuclei, the nonadiabatic couplings (NACs) and the energy-gap autocorrelation functions (EG-ACFs), can be analyzed. Two typical stages corresponding to the intramolecular vibrational relaxation and nonradiative transition processes are observed. We find that the combination of high frequency modes, like bond stretching, with low frequency modes, like the rotation around a double bond, is a more effective nonradiative channel in open-DPDBF than those that just contain the major contributions from the vibration modes with high frequencies in closed-DPDBF.

## II. Theoretical methods

### A. Electronic structure calculations

On-the-fly calculations of the electronic structure during the nonadiabatic dynamics have been performed in the framework of the DFTB method.<sup>62,63</sup> Both the Hamiltonian and atomic overlap matrices are parameterized as a function of the atomic distance and atom type. For the dynamic calculation, since the evolution of the integrals are no longer needed, the computations of the electronic structure are very efficient. It is convenient to transform the Hamiltonian into an orthonormal atomic basis through the Löwdin transformation and the Kohn–Sham (KS) equation can be simply written as,

$$\hat{H}_{\text{KS}}|\psi_i\rangle = \varepsilon_i|\psi_i\rangle \quad (1)$$

where  $\hat{H}_{\text{KS}}$  is the KS operator,  $\varepsilon_i$  is the  $i$ -th KS orbital with  $|\psi_i\rangle$  energy. After the expansion of the KS orbital on the orthonormal atomic orbitals, we obtain the corresponding matrix form  $H_{\text{KS}}C_i = C_i\varepsilon_i$ . The total energy of ground state reads:

$$E_{\text{GS}} = \sum_{i \in \text{occ}} n_i \varepsilon_i + U_{\text{rep}}, \quad (2)$$

where  $n_i$  is the occupation number of the  $i$ -th KS orbital and  $U_{\text{rep}}$  consists of the following contributions: exclusion of the double counting of electron repulsion in the first term of eqn (2), the electron exchange–correlation energy and the nuclear repulsion energy. It is expressed as a sum over the functions of atomic distance, is parameterized and termed as the effective nuclear repulsion energy.

Based on the KS orbitals from the DFTB, we could construct the adiabatic electronic states. In the single electron approximation,  $\hat{H}_e$  is defined as

$$\hat{H}_e = \sum_i \varepsilon_i (C_{i,\alpha}^\dagger C_{i,\alpha} + C_{i,\beta}^\dagger C_{i,\beta}), \quad (3)$$

where  $\alpha$  and  $\beta$  represent spin up and down, respectively,  $C_{i,\alpha}^\dagger$  and  $C_{i,\beta}^\dagger$  are creation operators and  $C_{i,\alpha}$  and  $C_{i,\beta}$  are annihilation operators. The excited state is expressed as a spin-adapted single excited Slater determinant by following Prezhdo's method,<sup>55</sup>

$$|\Phi_I\rangle \equiv |\Phi_k'\rangle = \frac{1}{\sqrt{2}}(C_{r,\alpha}^\dagger C_{k,\alpha} + C_{r,\beta}^\dagger C_{k,\beta})|\Phi_0\rangle, \quad (4)$$

where  $|\Phi_I\rangle$  is the  $I$ -th adiabatic electronic state,  $r$  and  $k$  represent the virtual and occupied KS orbitals, respectively,  $|\Phi_0\rangle$  is the ground electronic state  $|\psi_1\bar{\psi}_1 \cdots \psi_n\bar{\psi}_n\rangle$ , so the corresponding adiabatic energies for  $|\Phi_0\rangle$  and  $|\Phi_I\rangle$  are  $\sum_{i \in \text{occ}} 2\varepsilon_i$  and  $\sum_{i \in \text{occ}} 2\varepsilon_i - \varepsilon_k + \varepsilon_r$ , respectively.

### B. Nonadiabatic dynamics

In TSH, the trajectory of the nucleus follows the classical Newton equation of motion and the force at each time is given by one adiabatic state and the effective nuclear repulsion energy,  $U_{\text{rep}}$ . The force applied by the adiabatic state could be further calculated from the occupied KS orbitals in the following way:

$$\begin{aligned} M_l \ddot{\mathbf{R}}_l &= -\nabla_{\mathbf{R}_l} \langle \Phi_I | \hat{H}_e | \Phi_I \rangle - \nabla_{\mathbf{R}_l} U_{\text{rep}} \\ &= -\sum_i n_i \nabla_{\mathbf{R}_l} (C_i^\dagger H_{\text{KS}} C_i) - \nabla_{\mathbf{R}_l} U_{\text{rep}}, \\ &= -\sum_i n_i C_i^\dagger \nabla_{\mathbf{R}_l} H_{\text{KS}} C_i - \nabla_{\mathbf{R}_l} U_{\text{rep}}, \end{aligned} \quad (5)$$

where  $M_l$  and  $\mathbf{R}_l$  represent the mass and position for nucleus  $l$ , respectively. The repulsion term, which contains the double counting contributions from the electrons, could be obtained from the geometric structure. The  $\nabla_{\mathbf{R}_l} H_{\text{KS}}$  and  $\nabla_{\mathbf{R}_l} U_{\text{rep}}$  are evaluated by finite differentiation through displacing the nuclear position by  $5.0 \times 10^{-3}$  a.u. Under the framework of Tully's FSSH algorithm, during the integration of eqn (5), the quantum transitions among the adiabatic states are determined by the strength of the nonadiabatic couplings (NACs).

At time  $t$ , the time-evolving electronic state  $|\Phi(t)\rangle$  is defined as the superposition of the adiabatic electronic states

$$|\Phi(t)\rangle = \sum_I C_I(t) |\Phi_I\rangle, \quad (6)$$

The temporal evolution,  $|\Phi(t)\rangle$ , follows the time-dependent Schrödinger equation,

$$i\hbar \frac{\partial |\Phi(t)\rangle}{\partial t} = \hat{H}_e |\Phi(t)\rangle, \quad (7)$$

Then, the equation of motion for the electrons becomes:

$$\begin{aligned} \frac{\partial C_I(t)}{\partial t} &= (i\hbar)^{-1} C_I(t) E_I - \sum_J C_J(t) \langle \Phi_I | \frac{\partial}{\partial t} | \Phi_J \rangle \\ &= (i\hbar)^{-1} C_I(t) E_I - \sum_J C_J(t) \mathbf{D}_{IJ} \cdot \dot{\mathbf{R}}, \end{aligned} \quad (8)$$

where  $\mathbf{D}_{IJ}$  is the nonadiabatic coupling vectors (NACVs) between  $I$  and  $J$ . The NAC between the  $I$  and  $J$  states can be calculated numerically through

$$\begin{aligned} \left\langle \Phi_I \left( t + \frac{\Delta t}{2} \right) \left| \frac{\partial}{\partial t} \right| \Phi_J \left( t + \frac{\Delta t}{2} \right) \right\rangle &\approx \frac{1}{2\Delta t} (\langle \Phi_I(t) | \Phi_J(t + \Delta t) \rangle \\ &\quad - \langle \Phi_I(t + \Delta t) | \Phi_J(t) \rangle), \end{aligned} \quad (9)$$

where  $\Delta t$  is the time step for the nuclear motion. Generally, when solving eqn (8), the integration time step ( $\delta t$ ) for the electron is smaller than  $\Delta t$ , thus, we use the values for the NACs calculated from eqn (9) at time  $t - \Delta t/2$  and  $t + \Delta t/2$  and then apply a linear interpolation and extrapolation method to obtain the values at the interval  $t \sim t + \Delta t$ .

According to Tully's FSSH algorithm,<sup>74</sup> during the integration of eqn (8), the coefficients and NACs could be used to calculate the transition probability from  $I$  to  $J$  ( $P_{IJ}$ ) during the time step,  $\Delta t$ . The transition probability from  $I$  to other states at time  $t$  is

$$dP_I = \frac{da_{II}}{a_{II}} = \frac{\sum_{J(\neq I)} b_{JI}}{a_{II}} dt \equiv \sum_{J(\neq I)} dP_{IJ} \quad (10)$$

where  $a_{II} = C_I C_I^*$  and  $b_{JI} = -2\text{Re}(C_J C_I^* \mathbf{D}_{IJ} \cdot \dot{\mathbf{R}})$ .  $dP_{IJ}$  is a transition probability from  $I$  to  $J$  at time  $t$  as defined in eqn (10). During  $t$  to  $t + \Delta t$ , the transition probability from  $I$  to  $J$  is integrated and further approximated as a summation shown as follows:

$$P_{IJ}(t, \Delta t) = \int_t^{t+\Delta t} dt \frac{b_{JI}(t)}{a_{II}(t)} \approx \frac{\sum_{i=1}^N b_{JI}(i) \delta t}{a_{II}(t)} \quad (11)$$

Here,  $\sum_{J(\neq I)} b_{JI}$  denotes the flux of the occupation number ( $\dot{a}_{II}$ ) from state,  $N = \Delta t / \delta t$ . The transition probability is set to zero if it is negative. The hop from  $I$  to  $J$  could happen if

$$\sum_{K=1}^{J-1} P_{IK}(t, \Delta t) < \varepsilon < \sum_{K=1}^J P_{IK}(t, \Delta t) \quad (12)$$

where  $\varepsilon$  ( $0 \leq \varepsilon \leq 1$ ) is a uniform random number. After the hop, further velocity adjustment is needed.

$$\dot{\mathbf{R}}_I^J = \dot{\mathbf{R}}_I^I - \gamma_{\text{scale}} \frac{\mathbf{D}_{IJ}^I}{M_I}, \quad (13)$$

where  $\dot{\mathbf{R}}_I^I$  and  $\dot{\mathbf{R}}_I^J$  represent the nuclear ( $I$ ) velocities before and after the transition, respectively. The  $\gamma_{\text{scale}}$  is obtained according to the total energy conservation:

$$\gamma_{\text{scale}}^2 m_{IJ} - \gamma_{\text{scale}} n_{IJ} - (E_I - E_J) = 0, \quad (14)$$

where

$$m_{IJ} = \frac{1}{2} \sum_I \frac{(\mathbf{D}_{IJ}^I)^2}{M_I}, \quad (15)$$

$$n_{IJ} = \sum_I \mathbf{D}_{IJ}^I \cdot \dot{\mathbf{R}}_I. \quad (16)$$

If the kinetic energy available for the nuclei along the directions of the NACVs is not enough to jump over the electronic energy gap, that is, there does not exist a real solution for  $\gamma_{\text{scale}}$  in eqn (14), then the hop is rejected. Otherwise, a successful hop happens and then the nuclear velocities are adjusted along the NACV as shown in eqn (13). The NACV is calculated as follows:

$$\begin{aligned} \mathbf{D}_{IJ}^I &\equiv \langle \Phi_I | \hat{P} | \Phi_J \rangle \equiv \langle \Phi_I^s | \hat{P} | \Phi_J^r \rangle \\ &= -\delta_{rs} \langle \psi_k | \nabla_{\mathbf{R}_I} | \psi_l \rangle + \delta_{lk} \langle \psi_s | \nabla_{\mathbf{R}_I} | \psi_r \rangle, \end{aligned} \quad (17)$$

The KS orbital is expressed by the orthonormal atomic orbitals,

$$\begin{aligned} \langle \psi_j | \nabla_{\mathbf{R}_I} | \psi_i \rangle &= \sum_{\mu\nu} c_{\nu j}^* \nabla_{\mathbf{R}_I} c_{\mu i} \langle \phi_\nu | \phi_\mu \rangle + \sum_{\mu\nu} c_{\nu j}^* c_{\mu i} \langle \phi_\nu | \nabla_{\mathbf{R}_I} | \phi_\mu \rangle \\ &= C_j^\dagger \nabla_{\mathbf{R}_I} C_i + \sum_{\mu\nu} c_{\nu j}^* c_{\mu i} \langle \phi_\nu | \nabla_{\mathbf{R}_I} | \phi_\mu \rangle. \end{aligned} \quad (18)$$

Using the orthonormality of the eigenvector of the KS Hamiltonian, we get

$$(\nabla_{\mathbf{R}_I} C_j^\dagger) C_i = -C_j^\dagger \nabla_{\mathbf{R}_I} C_i. \quad (19)$$

For the off-diagonal term,

$$\nabla_{\mathbf{R}_I} (C_j^\dagger H_{\text{KS}} C_i) = \nabla_{\mathbf{R}_I} \delta_{ij} = 0, \quad (20)$$

$$\begin{aligned} \nabla_{\mathbf{R}_I} (C_j^\dagger H_{\text{KS}} C_i) &= (\nabla_{\mathbf{R}_I} C_j^\dagger) H_{\text{KS}} C_i + C_j^\dagger \nabla_{\mathbf{R}_I} H_{\text{KS}} C_i \\ &\quad + C_j^\dagger H_{\text{KS}} \nabla_{\mathbf{R}_I} C_i \\ &= (\varepsilon_j - \varepsilon_i) C_j^\dagger \nabla_{\mathbf{R}_I} C_i + C_j^\dagger \nabla_{\mathbf{R}_I} H_{\text{KS}} C_i, \end{aligned} \quad (21)$$

we obtain

$$C_j^\dagger \nabla_{\mathbf{R}_I} C_i = \frac{C_j^\dagger \nabla_{\mathbf{R}_I} H_{\text{KS}} C_i}{\varepsilon_i - \varepsilon_j} \quad (22)$$

For the second term,  $\sum_{\mu\nu} c_{\nu j}^* c_{\mu i} \langle \phi_\nu | \nabla_{\mathbf{R}_I} | \phi_\mu \rangle$  in eqn (18), when  $\mu = \nu$ , as

$$\begin{aligned} \nabla_{\mathbf{R}_I} \langle \phi_\mu | \phi_\mu \rangle &= 0 \\ &= \langle \nabla_{\mathbf{R}_I} \phi_\mu | \phi_\mu \rangle + \langle \phi_\mu | \nabla_{\mathbf{R}_I} \phi_\mu \rangle = 2 \langle \phi_\mu | \nabla_{\mathbf{R}_I} \phi_\mu \rangle, \end{aligned} \quad (23)$$

so

$$\langle \phi_\mu | \nabla_{\mathbf{R}_I} \phi_\mu \rangle = 0. \quad (24)$$

When  $\mu \neq \nu$ ,  $\langle \phi_\nu | \nabla_{\mathbf{R}_i} \phi_\mu \rangle$  is approximated to be zero, like the zero differential overlap approximation. Then, the second term is approximated to be zero.

Finally,

$$\langle \psi_j | \nabla_{\mathbf{R}_i} | \psi_i \rangle \approx \frac{C_j^\dagger \nabla_{\mathbf{R}_i} H_{KS} C_i}{\varepsilon_i - \varepsilon_j}. \quad (25)$$

The calculation of eqn (25) is similar to the nuclear force calculation in eqn (5).

The calculation of DFTB and the nuclear dynamics are performed using the semiclassical electron-radiation-ion dynamics (SERID)<sup>67,68</sup> program. We combined these with the electron dynamics as well as the FSSH algorithm by our own implementation.

### III. Results and discussion

#### A. Geometry optimization

Fig. 1 shows the geometries of open- and closed-DPDBF. The open-DPDBF is composed of one dibenzofulvene (DBF) and two benzene rings. The difference between the two molecules is that, in the open-DPDBF, the benzene ring can flexibly rotate around C33–C34, however, in the closed form, this position is locked by the bond between C12–C34. The optimizations for the ground state ( $S_0$ ) and the first excited state ( $S_1$ ) geometries of the two molecules are performed using DFT<sup>76</sup> and TDDFT<sup>77</sup> with the B3LYP functional and Gaussian basis set SV(P) (roughly 6-31G\*) in Turbomole.<sup>78,79</sup> The results are listed in Table 1. In both molecules, the major changes in the bond lengths from the  $S_0$  to  $S_1$  state are centered on the DBF rings. But the two twisting angles in open-DPDBF show about a 20° difference between the  $S_0$  and  $S_1$  states; however, there are no significant changes in the dihedral angles, such as those in C23=C21–C32=C20 in closed-DPDBF. These results are consistent with the electronic density redistribution from the highest occupied molecular orbital (HOMO) to the lowest unoccupied molecular orbital (LUMO) as reported in Fig. 2, which are calculated using the Gaussian 09 package with a B3LYP functional and 6-31G\* basis sets.<sup>80</sup>

**Table 1** Selected bond lengths (Å) and dihedral angles (degree) for open- and closed-DPDBF in  $S_0$  and  $S_1$

open-DPDBF	$S_0$	$S_1$
L(C33–C21)	1.37	1.44
L(C21–C11)	1.49	1.44
L(C21–C4)	1.49	1.44
L(C11–C16)	1.42	1.47
L(C4–C5)	1.42	1.47
L(C16–C5)	1.47	1.40
D(C22–C33=C21–C4)	19.7	40.5
D(C24=C22–C33=C21)	53.8	31.7
closed-DPDBF	$S_0$	$S_1$
L(C20–C32)	1.38	1.42
L(C32–C33)	1.46	1.43
L(C20–C4)	1.48	1.43
L(C11–C16)	1.42	1.46
L(C16–C5)	1.48	1.41
L(C4–C5)	1.43	1.48
D(C23=C21–C32=C20)	89.8	89.3

#### B. Nonadiabatic dynamics for the electrons and nuclei

We start the nonadiabatic dynamics from the optimized ground state structures of the two molecules, which are vertically excited from the HOMO to the LUMO. There are two electronic states,  $S_0$  and  $S_1$ , included in the dynamics. The initial velocities are sampled randomly according to the Boltzmann distribution with a temperature of 300 K. The electron equations of motion are solved by the fourth order Runge–Kutta method with a time step of  $10^{-3}$  fs, while the equations of motion for the nuclei are solved using the velocity Verlet algorithm with a time step of 1 fs. The total time scales for the simulations were 20 ps for open-DPDBF and 40 ps for closed-DPDBF. The evolution of the occupations averaged over the ensembles of 160 trajectories for the two molecules are shown in Fig. 3. The open-DPDBF is completely depopulated within 8 ps. The decay curve can be well described by a mono-exponential decay function and the fitted nonradiative lifetime is 1.4 ps. For closed-DPDBF, the simulation ends up at an  $S_1$  population of about 3%. The lifetime is fitted to be 24.5 ps, which is much slower than that of open-DPDBF. According to the experimental results,<sup>18</sup> the fluorescence quantum yields for open- and closed-DPDBF in acetonitrile are

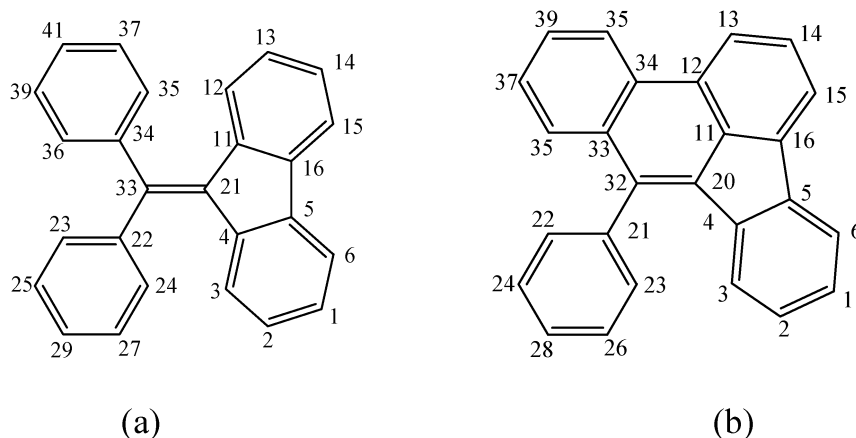


**Fig. 1** The chemical structures for (a) open- and (b) closed-DPDBF.



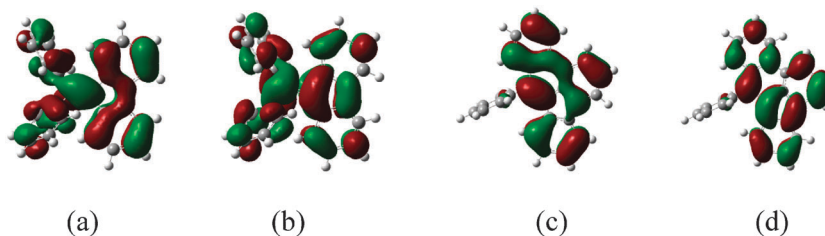


**Fig. 2** Frontier orbitals in the equilibrium geometries of the ground state: (a) HOMO (open-DPDBF), (b) LUMO (open-DPDBF), (c) HOMO (closed-DPDBF), (d) LUMO (closed-DPDBF).

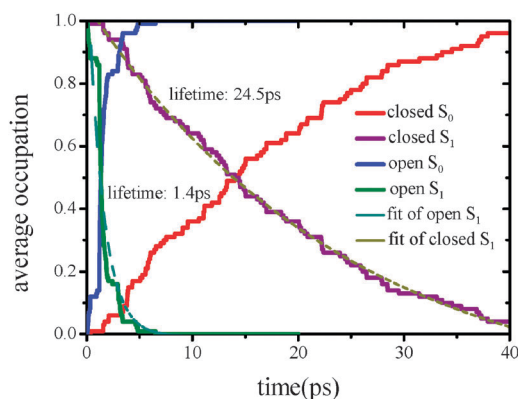


**Fig. 3** Average occupations from the ensembles of 160 trajectories of the nonadiabatic dynamics for open-DPDBF in  $S_0$  (blue) and  $S_1$  (green), closed-DPDBF in  $S_0$  (red) and  $S_1$  (purple). The mono-exponentially fitted decay lifetimes are 1.4 ps and 24.5 ps for open- and closed-DPDBF, respectively.

0.16% and 38%, respectively. It is expected that the nonradiative decay in the open form could be more than 200 times faster than in the closed form. Our results from the nonadiabatic dynamics are qualitatively in agreement with the experimental results; however, quantitatively, there is a discrepancy of about one order of magnitude with regards to the rate. A number of approximations, as follows, have been made in order to achieve a fast simulation on the 100 ps scale and this may cause such a discrepancy: (i) the solvent effect is neglected; (ii) the excited state is taken as the HOMO–LUMO orbital promotion; (iii) and the DFTB parameterization is adopted. Nevertheless, such a description still gives a reasonable account of the difference in the nonradiative decay in DPDBF.

Fig. 4 and 5 show the evolution of the energy gap between  $S_1$  and  $S_0$  averaged over 160 trajectories for open- and closed-DPDBF, respectively. As shown in Fig. 4, the energy gap with an initial value of 2.59 eV decays rapidly in the first 0.6 ps and, after some fluctuations, at  $\sim 1.1$  ps the gap goes back to about 2.5 eV. While for closed-DPDBF, as plotted in Fig. 5, a fast oscillation can be seen in the initial stage. The largest amplitude, which corresponds to an oscillation from 2.8 eV to 1.88 eV in the first several tens of femtoseconds and then again after  $\sim 2$  ps, decreases fast. After several tens of picoseconds, the energy gap increases slowly back to around 2.5 eV. In general, a low energy gap manifests a large nonadiabatic coupling between the two electronic states. Thus, the evolution of the energy gaps for the two compounds are consistent with the decay rates shown in Fig. 3. Some slow and fast oscillations in

the energy gap evolution curve also indicate the specific nuclear motions coupled to the electronic evolution processes. In particular, the low frequency oscillation in open-DPDBF could not be found in closed-DPDBF, suggesting the importance of the twisting of the bonds in the decay process of open-DPDBF.

Since there are too many degrees of freedom in the polyatomic molecules, it is difficult to trace the dynamics for all of them. According to the geometric changes between the optimized  $S_0$  and  $S_1$  states listed in Table 1, we can select a few typical bonds and dihedral angles, which change most notably from the excited state to the ground state for the two molecules. We plot the average values of these internal coordinates from the ensembles of the trajectories *versus* time in comparison with the energy gap evolution curve. The total average number of trajectories is 160. Fig. 4a shows the correlation between the double bond, C21=C33 (o- $R_1$ ), and the energy gap. After the initial excitation, the double bond length increases quickly from its initial value of 1.37 Å to 1.55 Å after 10 fs, then, before a time of  $\sim 1.1$  ps, it oscillates around 1.47 Å with a decreasing amplitude, which can be attributed to the intramolecular vibrational energy redistribution. This first stage coincides with a decrease in the energy gap. In the next few picoseconds, which corresponds to the nonradiative transition stage, the bond length vibrates back to  $\sim 1.38$  Å and the energy gap recovers back to  $\sim 2.5$  eV. To clearly see the changes in these two stages, the bond lengths were sampled as demonstrated in the inset of Fig. 4a. At about 1.05 ps and 10.37 ps, the stretching frequencies for the bond are calculated to be 1429  $\text{cm}^{-1}$  (23.3 fs) and 1814  $\text{cm}^{-1}$  (18.3 fs), respectively. The changes in the bond lengths and frequencies are in agreement with the restoration of a single bond to double bond. Fig. 4b illustrates the comparison of the temporal evolution of single bond C4–C21 (o- $R_2$ ) with the energy gap. For the whole period, the two curves possess very similar profiles. The inset in Fig. 4b shows that o- $R_2$  oscillates around 1.45 Å with a frequency of 1668  $\text{cm}^{-1}$  (20 fs) at  $\sim 0.93$  ps and 1.48 Å with a frequency of 1369  $\text{cm}^{-1}$  (24.4 fs) at  $\sim 7.42$  ps. The single bond length first decreases and then increases, which is opposite to the stretching motion of the double bond, o- $R_1$ , as seen in Fig. 4a. These dynamic changes in the bond length, which is concomitant with the electronic density redistribution, are consistent with the geometric differences between the  $S_0$  and  $S_1$  states obtained from the quantum chemistry optimization as listed in Table 1. The dihedral angle in C22–C33=C21–C4 (o- $\phi_1$ ) along with the energy gap evolution are plotted in Fig. 4c. The curve for o- $\phi_1$  is obtained from an average over the 121 trajectories, which covers the whole

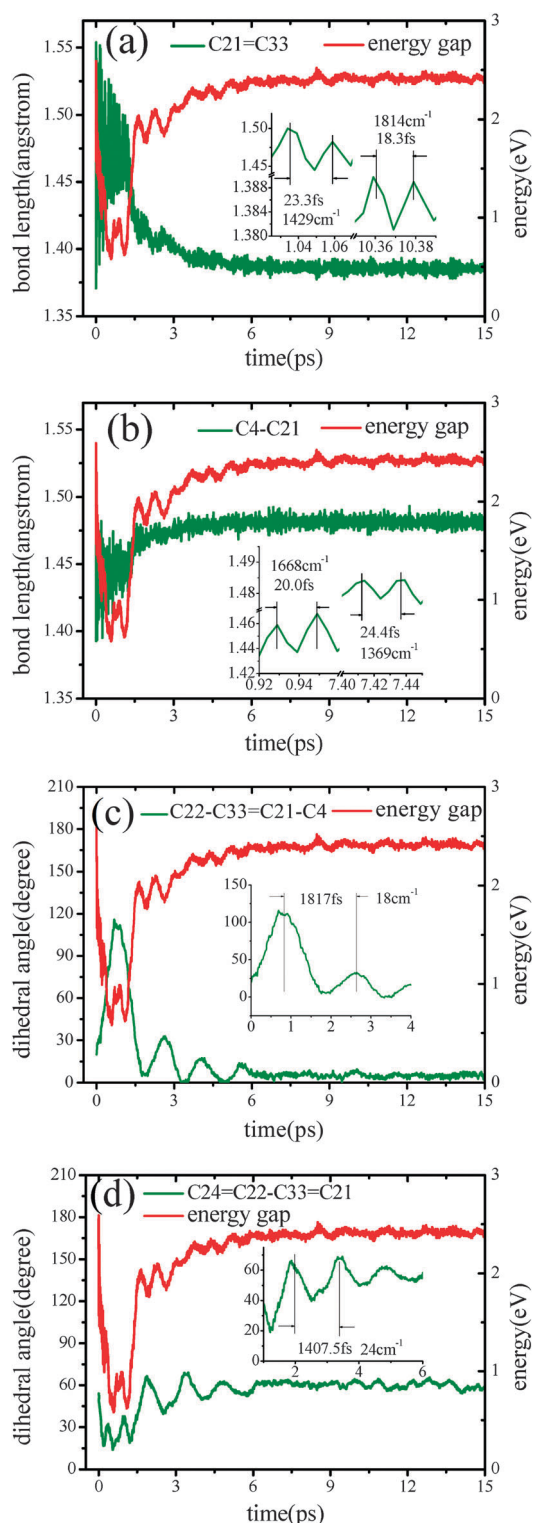


**Fig. 4** The temporal evolution of the energy gap ( $S_1-S_0$ ) (red) and the average values of the typical internal coordinates (a) C21=C33 (green), (b) C4-C21 (green), (c) C22-C33=C21-C4 (green), (d) C24=C22-C33=C21 (green) in open-DPDBF.

range of angle dynamics going back to the initial value. The data for the other angles with differences between their initial and final values greater than  $90^\circ$  are not shown. After the initial excitation, o- $R_1$  becomes a single bond and, thus, o- $\phi_1$

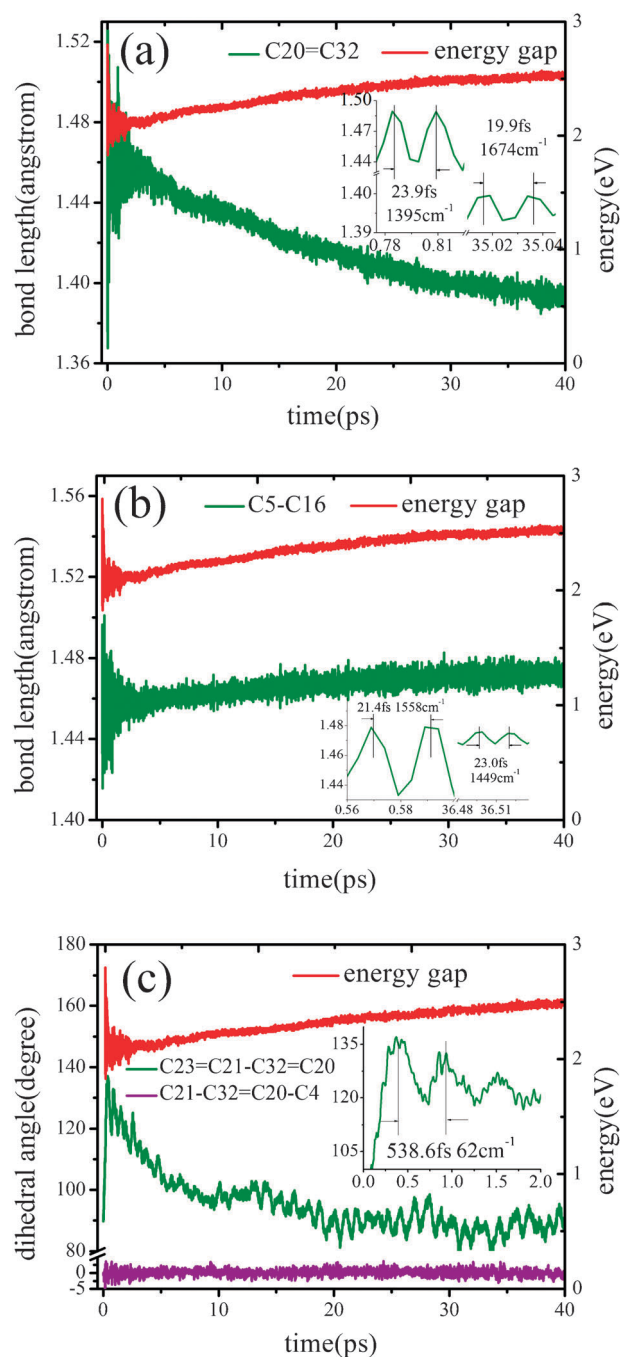


**Fig. 5** The temporal evolution of the energy gap ( $S_1-S_0$ ) (red) and the average values of the typical internal coordinates (a) C20=C32 (green), (b) C5-C16 (green), (c) C23=C21-C32=C20 (green), C21-C32=C20-C4 (purple) in closed-DPDBF.

can rotate around o- $R_1$  easily. When the energy gap peaks at  $\sim 0.6$  eV, o- $\phi_1$  rotates to its first maximum amplitude at  $\sim 110^\circ$ , which deviates about  $90^\circ$  from its initial value of  $19.7^\circ$ . While the energy gap recovers gradually in the second stage, o- $\phi_1$  rotates  $\sim 5^\circ$  with a decreasing amplitude, indicating the increasing planarity of the molecule after the vibrational relaxation process. The rotation frequency for o- $\phi_1$ , as shown in the inset of Fig. 4c, is estimated to be  $\sim 18$  cm $^{-1}$  (1817 fs). The single bond rotation for the dihedral

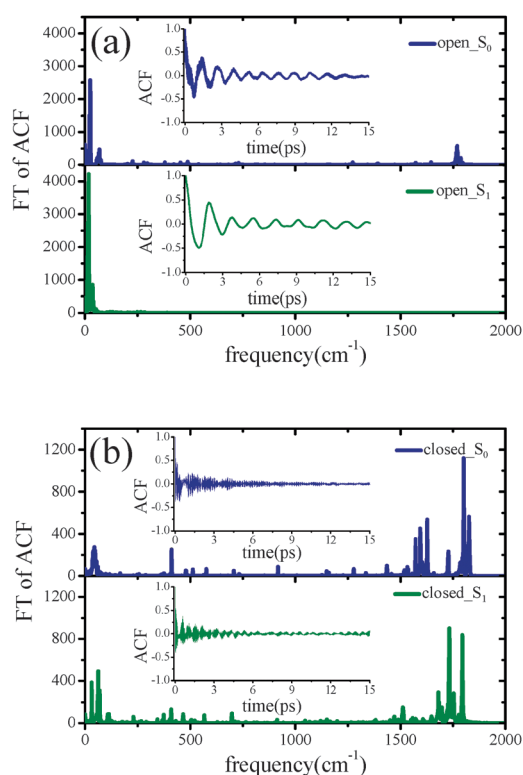


**Fig. 6** The Fourier transform of the energy gap ( $S_1-S_0$ ) autocorrelation functions (ACFs) from Born–Oppenheimer dynamics (a) open-DPDBF in  $S_0$  (upper panel, blue) and  $S_1$  (bottom panel, green), (b) closed-DPDBF in  $S_0$  (upper panel, blue) and  $S_1$  (bottom panel, green). The corresponding ACFs are shown in the insets.

angle in  $C24=C22-C33=C21$  ( $o-\phi_2$ ) and the energy gap are reported in Fig. 4d. The evolution profile for  $o-\phi_2$  is very similar to that of the energy gap; *e.g.* the position for the two minimum points appears at about 0.6 ps and the two stages correspond to decreasing and increasing processes. The inset in Fig. 4d gives an approximate twisting frequency of  $24\text{ cm}^{-1}$  (1407.5 fs) for  $o-\phi_2$ . The evolution reported here for the two bonds and dihedrals angles for the open form demonstrate the effective coupling of the typical high frequency stretching and the low frequency twisting motions with the electronic state evolution.

Now we discuss the evolution of the double bond,  $C20=C32$  ( $c-R_1$ ), and single bond  $C5-C16$  ( $c-R_2$ ) lengths in closed-DPDBF, as shown in Fig. 5a and b, respectively. Similar to open-DPDBF, closed-DPDBF also has two stages during the excited state decay process. First, immediately after the initial excitation, the bond lengths change in less than 10 fs and then stretch around the new equilibrium lengths in the following 2.5 ps, with decreasing amplitudes. This stage is consistent with the fast decreasing energy gap and the following oscillation around 2.1 eV. During this stage,  $c-R_1$  increases to about 1.46 Å from 1.38 Å, while  $c-R_2$  decreases to about 1.46 Å from 1.48 Å. In the second stage, which corresponds to the nonadiabatic transition process, the bonds relax to their ground state geometries gradually. The slowly increasing energy gap corresponds to this stage. Typical frequencies for  $c-R_1$  in the two stages, as shown in the inset of Fig. 5a, are

$1395\text{ cm}^{-1}$  (23.9 fs) and  $1674\text{ cm}^{-1}$  (19.9 fs), respectively. And for  $c-R_2$  the first stage has a frequency of  $1558\text{ cm}^{-1}$  (21.4 fs) and the second stage has a frequency of  $1449\text{ cm}^{-1}$  (23.0 fs). Both changes in the frequencies are consistent with the bond length evolution. The time evolution curves for the dihedral angle in  $C23=C21-C32=C20$  ( $c-\phi_1$ ) and  $C21-C32=C20-C4$  ( $c-\phi_2$ ) are plotted in Fig. 5c. The curve for  $c-\phi_1$  is obtained from an average over 86 trajectories, which corresponds to 54% of the total 160 trajectories, since either clockwise or anticlockwise rotations around the single  $C21-C32$  bond may be possible. For  $c-\phi_1$ , the initial increase of the angle from  $89.8^\circ$  to about  $137^\circ$  coincides with a decreasing energy gap; however, in the following nonadiabatic decay process, the angle decreases faster than the recovery speed of the energy gap. The frequency for the rotation is estimated to be  $62\text{ cm}^{-1}$  (538.6 fs) as shown in the inset of Fig. 5c. The lack of concomitant correspondence with the energy gap evolution indicates that the contribution of  $c-\phi_1$  to the gap is minor compared to the high frequency modes. For  $c-\phi_2$  twisting around  $c-R_1$ , due to the locking of the benzene ring by the  $C34-C12$  bond, the amplitude for the oscillation is about  $5^\circ$ , which is significantly smaller than that of  $o-\phi_1$  in Fig. 4c. The evolution for the typical internal coordinates shown here indicate that, in closed-DPDBF, the stretching vibrations are more important than the low frequency twisting rotations in the sense of coupling with electronic motions.

### C. Born–Oppenheimer dynamics

To further illustrate the relative contributions of the vibrational modes in accepting the excess energy during the nonradiative decay process, we start with Born–Oppenheimer dynamics on the  $S_0$  and  $S_1$  state potential energy surfaces (PES). The results are obtained from 80 trajectories with nuclear time steps of 0.25 fs. The energy gap autocorrelation function (EG\_ACF) is calculated as:

$$\text{EG\_ACF} = \frac{\langle C_{EE}(n\Delta t) \rangle}{\langle C_{EE}(0) \rangle}, \quad (26)$$

where

$$C_{EE}(n\Delta t) = \frac{1}{M-n} \sum_{m=1}^{M-n} E_{\text{gap}}(m\Delta t) E_{\text{gap}}((m+n)\Delta t), \quad (27)$$

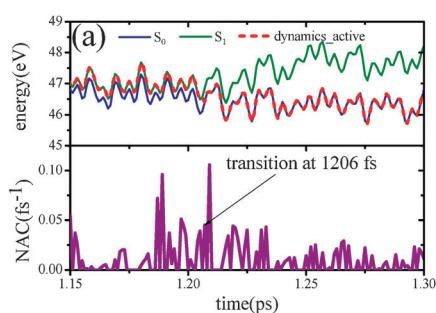
$E_{\text{gap}}$  is the energy gap between  $S_1$  and  $S_0$ ,  $\Delta t$  is the nuclear time step and  $M$  is the total sampling point. The initial sampling for the geometries and velocities was the same as the nonadiabatic dynamics. Fig. 6a and b show the EG-ACFs and the Fourier transform (FT) results for open- and closed-DPDBF, respectively. The EG-ACFs reflect the typical modes coupling to the energy gap and their FT results have can be directly related to the reorganization energy. The results for the  $S_0$  state reported in the top panel of Fig. 6a indicate that the major contribution comes from the low frequency region ( $\sim 30\text{ cm}^{-1}$ ), which is consistent with a low frequency rotation, as shown in Fig. 4c. A minor contribution from a mode at  $\sim 1770\text{ cm}^{-1}$  can be attributed to the  $C=C$  stretching vibration ( $\nu_{C=C}$ ). For the  $S_1$  state shown in the lower panel of Fig. 6a, nearly all the peaks are located in the low frequency region. The disappearance of the peak at  $\nu_{C=C}$  may be caused by the transition of the double



bond to a single bond in the  $S_1$  state, which is overwhelmed by the contributions from the modes with low frequencies. Comparing the EG-ACFs, as illustrated in the inset of each panel in Fig. 6a, we found that both curves show an initial decay within about 0.4 ps, suggesting memory loss of the initial energy gap, which is possibly caused by the thermal fluctuation. The following slow periodic oscillations in both cases indicate the energy gaps are modulated by low frequency modes. However, in the case of the  $S_0$  state, the high frequency modes also contribute to the oscillation, which is consistent with the FT results. For closed-DPDBF, shown in Fig. 6b, the high frequency modes with peak positions ranging from 1550 to 1800  $\text{cm}^{-1}$  give major contributions in both  $S_0$  and  $S_1$ . The small peaks with locations at about 50  $\text{cm}^{-1}$  come from the single bond ( $\text{C}-\phi_1$ ) rotation according to results shown in Fig. 5c. The insets in the upper and lower panels of Fig. 6b show the evolution for the EG-ACFs. It is observed that the high frequency modes play a more important role in the modulation of the energy gap. The small oscillations with low frequencies can be found in the  $S_1$  state but are not significant in  $S_0$ , so the low frequency modes give relatively high fractions in the FT results compared to those in  $S_0$ .

#### D. Typical trajectory analysis

We report the evolution of the PES, NACs and NACVs from a typical single trajectory for open-DPDBF in Fig. 7. As shown in the upper panel of Fig. 7a, close to the transition



(b)

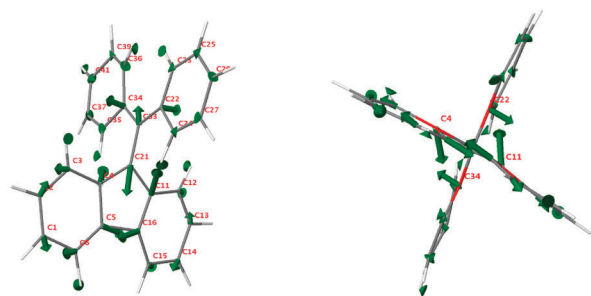
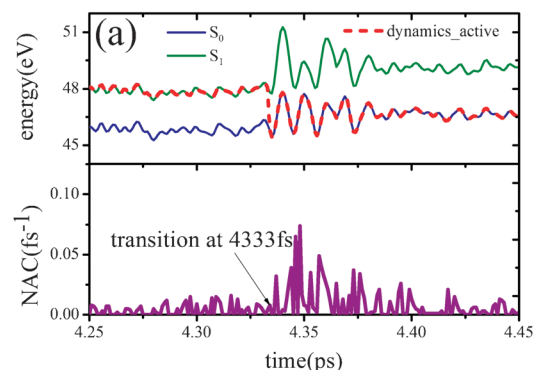


**Fig. 7** Analysis of a typical single trajectory analysis with a transition at 1206 fs for open-DPDBF (a) electronic state energy (upper panel) for  $S_0$  (blue),  $S_1$  (green) and the dynamics (denoted as dynamics\_active, red) versus time and the absolute values of the nonadiabatic couplings (NACs) (bottom panel, purple) versus time. (b) The nonadiabatic coupling vectors (NACVs) and the geometric structure at 1206 fs, the left hand side gives an overall view while the right hand side shows the side view to highlight the NACVs on the atoms C4, C11, C22, C34 with rotation around the double bond ( $\text{C21}=\text{C33}$ ).

point at 1206 fs, the energy for the  $S_0$  and  $S_1$  states approach each other with a gap of less than 0.5 eV and, after hopping, the energy gap becomes gradually larger. The absolute values for the NACs between  $S_0$  and  $S_1$  are plotted in the bottom panel. The intensity is relatively large when the gap becomes small suggesting a strong nonadiabatic coupling between the two states. The geometry and NACVs that promote the transition at 1206 fs are shown in Fig. 7b. It should be noticed that the lengths of the NACVs are proportional to their actual magnitudes. At the transition point, the two benzene rings are nearly coplanar and the DBF ring is approximately perpendicular to the two rings. The NACVs, with a major part centering on the DBF ring, typically give in-plane vibrations, as can be seen on the left in Fig. 7b. In particular, as shown on the right in Fig. 7b, if a side view of the molecule is taken, the vectors on the four atoms C4, C11, C22 and C34 twist around the bond,  $\text{o}-\text{R}_1$ , which is in agreement with the results in Fig. 4c.

In the case of closed-DPDBF, the evolution of the PES, NACs and NACVs from a typical single trajectory are reported in Fig. 8. In contrast to open-DPDBF, the energy gap is relatively large at  $\sim 2$  eV, even close to the transition point (4333 fs), as can be seen in the upper panel of Fig. 8a. So, as shown in the bottom panel, it is reasonable that the NACs are relatively small in comparison with those of open-DPDBF before the transition. In Fig. 8b, the geometric structure with



(b)

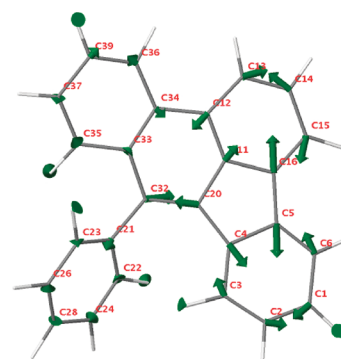


**Fig. 8** Analysis of a typical single trajectory with a transition at 4333 fs for closed-DPDBF (a) electronic state energy (top panel) for  $S_0$  (blue),  $S_1$  (green) and the dynamics (denoted as dynamics\_active, red) versus time and the nonadiabatic couplings (NACs) (bottom panel, purple) versus time. (b) The nonadiabatic coupling vectors (NACVs) and the geometric structure at 4333 fs.



the NACVs at the transition point is shown. It is easy to note that the major contribution is from the in-plane vibration of the DBF ring and the stretching motion of c-R<sub>1</sub>. This result indicates the importance of the high frequency modes in promoting a transition in closed-DPDBF. Similar to open-DPDBF, the absolute lengths for the NACVs are also proportional to the actual magnitudes.

#### IV. Conclusions

We have carried out a nonadiabatic dynamics simulation for the excited state nonradiative decay processes in open- and closed-DPDBF and we have shown that the former exhibits an exotic aggregation induced emission property in sharp contrast to the normal aggregation quenching of the latter. From the geometry optimizations in the S<sub>0</sub> and S<sub>1</sub> states, we found that, in both molecules, the major bond lengths modifications appear in the DBF ring. The typical dihedral angle changes, such as o-φ<sub>1</sub> and o-φ<sub>2</sub> in open-DPDBF, are about 20°. In closed-DPDBF, the dihedral angles do not show any significant modification. In open-DPDBF, both the bond stretching in the DBF ring and the ring rotation around the double bond play essential roles in the electronic nonadiabatic transition. In closed-DPDBF, the major contributions come from the bond stretching in the DBF ring and this relates to both accepting energy and in the promotion of the NACs. In both molecules, the single bond twist is effective in accepting energy but not in promoting the NACs. The EG-ACFs from Born–Oppenheimer dynamics illustrate the relative contributions to the reorganization energy from the vibrational mode relaxations. In open-DPDBF, the major contributions come from the low frequency twisting modes, while the high frequency stretching modes are more important in closed-DPDBF. In general, the larger the reorganization energy, the more important the mode is in accepting energy in the nonradiative decay process. So, during the nonradiative decay process, open-DPDBF manifests larger changes in the energy gap and faster decay rates than those in closed-DPDBF, which is qualitatively consistent with experimental results.

Though our investigation is, so far, confined to the single molecule nonradiative decay process, the theoretical findings do rationalize the AIE effect of open-DPDBF in the solid phase. This is because open-DPDBF shows no significant change in the profile and position of the absorption spectrum during the aggregation process.<sup>18</sup> Thus, the formation of J-aggregates or excitonics could be a minor occurrence. When the molecules go from a dilute solution to an aggregate, the low frequency rotation modes are easily restricted and the nonradiative channel is blocked. The incorporation of environmental effects, such as the surrounding molecules, through the QM/MM method with nonadiabatic dynamics is being actively pursued.

#### Acknowledgements

Prof. Yushen Dou is greatly acknowledged for providing us with the SERID code for DFTB and the nuclear dynamics section. This work was supported by the National Natural Science Foundation of China (Grant No. 90921007, 20903102

and 21103097) and the Ministry of Science and Technology of China through the 973 program (Grant No. 2009CB623600, 2011CB932304, 2011CB808405).

#### References

- 1 Y. Hong, J. W. Y. Lam and B. Z. Tang, *Chem. Commun.*, 2009, 4332.
- 2 Y. Hong, J. W. Y. Lam and B. Z. Tang, *Chem. Soc. Rev.*, 2011, **40**, 5361.
- 3 Z. Ning and H. Tian, *Chem. Commun.*, 2009, 5483.
- 4 H. C. Yeh, S. J. Yeh and C. T. Chen, *Chem. Commun.*, 2003, 2632.
- 5 Z. Zhao, S. Chen, J. W. Y. Lam, P. Lu, Y. Zhong, K. S. Wong, H. S. Kwok and B. Z. Tang, *Chem. Commun.*, 2010, **46**, 2221.
- 6 Y. Hong, C. Feng, Y. Yu, J. Liu, J. W. Y. Lam, K. Q. Luo and B. Z. Tang, *Anal. Chem.*, 2010, **82**, 7035.
- 7 J. Liu, Y. Zhong, P. Lu, Y. Hong, J. W. Y. Lam, M. Faisal, Y. Yu, K. S. Wong and B. Z. Tang, *Polym. Chem.*, 2010, **1**, 426.
- 8 Y. Liu, Y. Tang, N. N. Barashkov, I. S. Irgibaeva, J. W. Y. Lam, R. Hu, D. Birimzhanova, Y. Yu and B. Z. Tang, *J. Am. Chem. Soc.*, 2010, **132**, 13951.
- 9 Y. Liu, C. Deng, L. Tang, A. Qin, R. Hu, J. Z. Sun and B. Z. Tang, *J. Am. Chem. Soc.*, 2011, **133**, 660.
- 10 T. Sanji, K. Shiraishi and M. Tanaka, *ACS Appl. Mater. Interfaces*, 2009, **1**, 270.
- 11 M. Zhao, M. Wang, H. Liu, D. Liu, G. Zhang, D. Zhang and D. Zhu, *Langmuir*, 2009, **25**, 676.
- 12 M. Faisal, Y. Hong, J. Liu, Y. Yu, J. W. Y. Lam, A. Qin, P. Lu and B. Z. Tang, *Chem.–Eur. J.*, 2010, **16**, 4266.
- 13 F. Mahtab, Y. Yu, J. W. Y. Lam, J. Liu, B. Zhang, P. Lu, X. Zhang and B. Z. Tang, *Adv. Funct. Mater.*, 2011, **21**, 1733.
- 14 Y. Yu, C. Feng, Y. N. Hong, J. Z. Liu, S. J. Chen, K. M. Ng, K. Q. Luo and B. Z. Tang, *Adv. Mater.*, 2011, **23**, 3298.
- 15 J. D. Luo, Z. L. Xie, J. W. Y. Lam, L. Cheng, H. Y. Chen, C. F. Qiu, H. S. Kwok, X. W. Zhan, Y. Q. Liu, D. B. Zhu and B. Z. Tang, *Chem. Commun.*, 2001, 1740.
- 16 Z. Zhao, P. Lu, J. W. Y. Lam, Z. Wang, C. Y. K. Chan, H. H. Y. Sung, I. D. Williams, Y. Ma and B. Z. Tang, *Chem. Sci.*, 2011, **2**, 672.
- 17 H. Tong, Y. Q. Dong, M. Haussler, J. W. Y. Lam, H. H. Y. Sung, I. D. Williams, J. Z. Sun and B. Z. Tang, *Chem. Commun.*, 2006, 1133.
- 18 H. Tong, Y. Dong, Y. Hong, M. Haussler, J. W. Y. Lam, H. H. Y. Sung, X. Yu, J. Sun, I. D. Williams, H. S. Kwok and B. Z. Tang, *J. Phys. Chem. C*, 2007, **111**, 2287.
- 19 S. W. Yin, Q. Peng, Z. Shuai, W. H. Y. Fang, Y. H. Wang and Y. Luo, *Phys. Rev. B: Condens. Matter Mater. Phys.*, 2006, **73**, 205409.
- 20 Q. Peng, Y. Yi, Z. Shuai and J. Shao, *J. Chem. Phys.*, 2007, **126**, 114302.
- 21 Y. Niu, Q. Peng and Z. Shuai, *Sci. China, Ser. B: Chem.*, 2008, **51**, 1153.
- 22 Q. Peng, Y. Yi, Z. Shuai and J. Shao, *J. Am. Chem. Soc.*, 2007, **129**, 9333.
- 23 Q. Peng, Y. Niu, C. Deng and Z. Shuai, *Chem. Phys.*, 2010, **370**, 215.
- 24 C. Deng, Y. Niu, Q. Peng, A. Qin, Z. Shuai and B. Z. Tang, *J. Chem. Phys.*, 2011, **135**, 14304.
- 25 Y. Niu, Q. Peng, C. Deng, X. Gao and Z. Shuai, *J. Phys. Chem. A*, 2010, **114**, 7817.
- 26 Q. Y. Wu, C. M. Deng, Q. Peng, Y. L. Niu and Z. G. Shuai, DOI: 10.1021/jp3002367.
- 27 F. Webster, P. J. Rossky and R. A. Friesner, *Comput. Phys. Commun.*, 1991, **63**, 494.
- 28 J. C. Tully, *Faraday Discuss.*, 1998, **110**, 407.
- 29 J. C. Tully, *Nonadiabatic Dynamics*, in *Modern methods for multi-dimensional dynamics computations in chemistry*, ed. D. L. Thompson, World Scientific, Singapore, 1998, pp. 34–72.
- 30 N. L. Doltsinis and D. Marx, *J. Theor. Comput. Chem.*, 2002, **1**, 319.
- 31 A. W. Jasper, S. Nangia, C. Y. Zhu and D. G. Truhlar, *Acc. Chem. Res.*, 2006, **39**, 101.
- 32 M. Barbatti, *Wiley Interdiscip. Rev.: Comput. Mol. Sci.*, 2011, **1**, 620.

- 33 M. Barbatti and H. Lischka, *J. Am. Chem. Soc.*, 2008, **130**, 6831.
- 34 T. Ishida, S. Nanbu and H. Nakamura, *J. Phys. Chem. A*, 2009, **113**, 4356.
- 35 M. Barbatti, A. J. A. Aquino, J. J. Szymczak, D. Nachtigallova, P. Hobza and H. Lischka, *Proc. Natl. Acad. Sci. U. S. A.*, 2010, **107**, 21453.
- 36 W. C. Chung, S. Nanbu and T. Ishida, *J. Phys. Chem. A*, 2010, **114**, 8190.
- 37 M. Barbatti, A. J. A. Aquino, J. J. Szymczak, D. Nachtigallova and H. Lischka, *Phys. Chem. Chem. Phys.*, 2011, **13**, 6145.
- 38 M. Barbatti, J. J. Szymczak, A. J. A. Aquino, D. Nachtigallova and H. Lischka, *J. Chem. Phys.*, 2011, **134**, 014304.
- 39 D. Nachtigallova, A. J. A. Aquino, J. J. Szymczak, M. Barbatti, P. Hobza and H. Lischka, *J. Phys. Chem. A*, 2011, **115**, 5247.
- 40 J. Cao, Q. Fang and W. Fang, *J. Chem. Phys.*, 2011, **134**, 44307.
- 41 G. Cui and W. Fang, *J. Phys. Chem. A*, 2011, **115**, 1547.
- 42 G. Cui and W. Fang, *J. Phys. Chem. A*, 2011, **115**, 11544.
- 43 A. Kazaryan, Z. Lan, L. V. Schafer, W. Thiel and M. Filatov, *J. Chem. Theory Comput.*, 2011, **7**, 2189.
- 44 Z. Lan, E. Fabiano and W. Thiel, *J. Phys. Chem. B*, 2009, **113**, 3548.
- 45 O. Weingart, Z. Lan, A. Koslowski and W. Thiel, *J. Phys. Chem. Lett.*, 2011, **2**, 1506.
- 46 S. Fernandez-Alberti, V. D. Kleiman, S. Tretiak and A. E. Roitberg, *J. Phys. Chem. Lett.*, 2010, **1**, 2699.
- 47 T. Nelson, S. Fernandez-Alberti, V. Chernyak, A. E. Roitberg and S. Tretiak, *J. Phys. Chem. B*, 2011, **115**, 5402.
- 48 C. Ciminelli, G. Granucci and M. Persico, *Chem.-Eur. J.*, 2004, **10**, 2327.
- 49 T. Cusati, G. Granucci and M. Persico, *J. Am. Chem. Soc.*, 2011, **133**, 5109.
- 50 E. Tapavicza, I. Tavernelli and U. Rothlisberger, *Phys. Rev. Lett.*, 2007, **98**, 23001.
- 51 E. Tapavicza, I. Tavernelli, U. Rothlisberger, C. Filippi and M. E. Casida, *J. Chem. Phys.*, 2008, **129**, 124108.
- 52 U. Werner, R. Mitric, T. Suzuki and V. Bonacic-Koutecky, *Chem. Phys.*, 2008, **349**, 319.
- 53 M. Wohlgemuth, V. Bonacic-Koutecky and R. Mitric, *J. Chem. Phys.*, 2011, **135**, 54105.
- 54 O. V. Prezhdo, *Acc. Chem. Res.*, 2009, **42**, 2005.
- 55 C. F. Craig, W. R. Duncan and O. V. Prezhdo, *Phys. Rev. Lett.*, 2005, **95**, 163001.
- 56 W. R. Duncan and O. V. Prezhdo, *Annu. Rev. Phys. Chem.*, 2007, **58**, 143.
- 57 S. A. Fischer, B. F. Habenicht, A. B. Madrid, W. R. Duncan and O. V. Prezhdo, *J. Chem. Phys.*, 2011, **134**, 24102.
- 58 O. V. Prezhdo, W. R. Duncan and V. V. Prezhdo, *Prog. Surf. Sci.*, 2009, **84**, 30.
- 59 N. L. Doltsinis and D. Marx, *Phys. Rev. Lett.*, 2002, **88**, 166402.
- 60 P. R. L. Markwick and N. L. Doltsinis, *J. Chem. Phys.*, 2007, **126**, 175102.
- 61 H. Nieber, A. Hellweg and N. L. Doltsinis, *J. Am. Chem. Soc.*, 2010, **132**, 1778.
- 62 M. Elstner, *Theor. Chem. Acc.*, 2006, **116**, 316.
- 63 M. Elstner, D. Porezag, G. Jungnickel, J. Elsner, M. Haugk, T. Frauenheim, S. Suhai and G. Seifert, *Phys. Rev. B: Condens. Matter*, 1998, **58**, 7260.
- 64 T. Frauenheim, G. Seifert, M. Elstner, Z. Hajnal, G. Jungnickel, D. Porezag, S. Suhai and R. Scholz, *Phys. Status Solidi B*, 2000, **217**, 41.
- 65 T. A. Niehaus, S. Suhai, F. Della Sala, P. Lugli, M. Elstner, G. Seifert and T. Frauenheim, *Phys. Rev. B: Condens. Matter*, 2001, **63**, 85108.
- 66 R. Mitric, U. Werner, M. Wohlgemuth, G. Seifert and V. Bonacic-Koutecky, *J. Phys. Chem. A*, 2009, **113**, 12700.
- 67 R. E. Allen, *Phys. Rev. B: Condens. Matter*, 1994, **50**, 18629.
- 68 Y. S. Dou, B. R. Torralva and R. E. Allen, *J. Mod. Optic.*, 2003, **50**, 2615.
- 69 C. Jiang, X. Zhou, Z. Lin, R. Xie, F. Li, M. Gao and R. E. Allen, *Phys. Status Solidi B-Basic Solid State Physics.*, 2011, **248**, 2008.
- 70 Y. Lei, S. Yuan, Y. Dou, Y. Wang and Z. Wen, *J. Phys. Chem. A*, 2008, **112**, 8497.
- 71 W. Y. Zhang, S. A. Yuan, A. Y. Li, Y. S. Dou, J. S. Zhao and W. H. Fang, *J. Phys. Chem. C*, 2010, **114**, 5594.
- 72 P. V. Parandekar and J. C. Tully, *J. Chem. Phys.*, 2005, **122**, 94102.
- 73 P. V. Parandekar and J. C. Tully, *J. Chem. Theory Comput.*, 2006, **2**, 229.
- 74 S. Hammes-Schiffer and J. C. Tully, *J. Chem. Phys.*, 1994, **101**, 4657.
- 75 J. C. Tully, *J. Chem. Phys.*, 1990, **93**, 1061.
- 76 M. Haser and R. Ahlrichs, *J. Comput. Chem.*, 1989, **10**, 104.
- 77 F. Furche and R. Ahlrichs, *J. Chem. Phys.*, 2002, **117**, 7433.
- 78 R. Ahlrichs, M. Bar, M. Haser, H. Horn and C. Kolmel, *Chem. Phys. Lett.*, 1989, **162**, 165.
- 79 TURBOMOLE V6.3, TURBOMOLE GmbH, Karlsruhe, 2011; available from <http://www.turbomole.com>.
- 80 M. J. Frisch, *et al.*, *GAUSSIAN 09 Revision A.02*, Gaussian, Inc., Wallingford CT, 2009.